



Experimental study of boiling heat transfer in a microchannel with nucleated-shape columnar micro-pin-fins

Wun-Rong Liao^a, Liang-Han Chien^{b,c}, Mohammad Ghalambaz^{d,e}, Wei-Mon Yan^{b,c,*}

^a National Synchrotron Radiation Research Center, Hsin-Chu 300, Taiwan

^b Department of Energy and Refrigerating Air-Conditioning Engineering, National Taipei University of Technology, Taipei 10608, Taiwan

^c Research Center of Energy Conservation for New Generation of Residential, Commercial, and Industrial Sectors, National Taipei University of Technology, Taipei 10608, Taiwan

^d Department for Management of Science and Technology Development, Ton Duc Thang University, Ho Chi Minh City, Vietnam

^e Faculty of Applied Sciences, Ton Duc Thang University, Ho Chi Minh City, Vietnam

ARTICLE INFO

Keywords:

Microchannel

Flow boiling

Parallel nucleate micro-pin-fin

ABSTRACT

The boiling regime and flow field patterns of boiling heat transfer of FC-72 dielectric fluid in a microchannel are experimentally studied. The inner surface of the test section of the microchannel is covered with nucleated columnar fins of height 100 μm . Each fin is nucleated with the core diameter of 60 μm and opening of 45 μm , which the fin openings is aligned opposite to the flow direction. The experiments are performed for two saturation temperatures of $T_{\text{sat}} = 35^\circ\text{C}$ and $T_{\text{sat}} = 50^\circ\text{C}$. The heat flux and mass velocity are in the range of 0.67–4.5 W/cm^2 , and 94–138 $\text{kg}/\text{m}^2\text{s}$, respectively. The results are reported for the on boiling temperature difference and pressure drop. The flow-field behavior of formation of bubbles at the nucleated fins, single-pore nucleation, and boiling flow regime are addressed. The results reveal that the increase in the mass velocity increases the subcooled temperature difference. The flow-behavior images in the test-section show that cell flow, block flow, droplet/block flow, droplet flow, and annular flow patterns can be formed by the increase of the surface heat flux. The on boiling phase change induces about three-fold of pressure-drop in the microchannel. Besides, the rise of the working fluid saturation temperature raises the pressure-drop.

1. Introduction

Heat dissipation is crucial for the proper performance of high-density optical devices, microelectronics, chipsets, and other devices. In aerospace applications, heat removal is critically important due to the harsh surrounding environment and enclosed internal systems. Spaceborne vehicles, satellites, and avionics all rely upon their thermal control systems to adjust the working temperature of the power systems, communication systems, instruments, and other electronic devices within a safe working-temperature range. Study of conventional thermal management systems shows that many of these systems rely on the conductance of thermal energy to absorb the heat from warm components and reject it to heat exchangers, radiators or other cold components [1].

The growing use of high-performance electronics, communication systems, and spaceborne instruments has increased the thermal load and surface heat flux density of components. Further advance cooling systems with high efficiency and low weights for handling high surface

heat fluxes are demanded due to the weight and size constraints in satellite systems [1]. Furthermore, some thermal sensitive devices such as lasers [2], optical alignment systems [3], and detectors [4] require accurate temperature-control with a limited temperature difference.

Using the evaporative cooling is a new advanced cooling method that can further enhance the heat capacity and efficiency of heat removal systems with tight temperature regulation. It can also reduce the weight of heatsinks, which is an excellent advantage for satellite and aerospace applications. Hardesty [1] has invented a microchannel heatsink, which evaporates a part of the coolant to cool the surface of the heatsink, and then, it utilizes the vapor as a driving mean to produce a flowing current in the heatsink. The evaporation process absorbs much heat from the heat source in almost a constant temperature. Hence, in evaporative systems employing a limited temperature difference between the heat source and the coolant is applicable. A microchannel typically consists of many small channels-ducts over a thermally conductive surface, which is in contact with a plan surface mounted over a heat source. The small channels allow high thermal

* Corresponding author at: Department of Energy and Refrigerating Air-Conditioning Engineering, National Taipei University of Technology, Taipei 10608, Taiwan.
E-mail addresses: mohammad.ghalambaz@tdtu.edu.vn (M. Ghalambaz), wmyan@ntut.edu.tw (W.-M. Yan).

Nomenclature

A_c	Cross-sectional area of the microchannel (m^2)	P_i	Inlet pressure of the test section (kPa)
A_p	Projected area (m^2)	P_o	Outlet pressure of the test section (kPa)
C_p	Specific heat capacity of the fluid ($\text{J/kg}^\circ\text{C}$)	Q	Input power (W)
G	Mass velocity ($\text{kg/m}^2\text{s}$)	q''	Surface heat flux ($\text{W/m}^2\text{K}$)
h_{fg}	The enthalpy of phase change from liquid to vapor (J/kg)	Q_{loss}	Heat loss (W)
k	Thermal conductivity of the microchannel	T	Temperature ($^\circ\text{C}$)
k_f	Thermal conductivity of the fluid ($\text{W/m}^\circ\text{C}$)	T_{in}	Inlet temperature of the fluid ($^\circ\text{C}$)
\dot{m}	The mass flow rate (kg/s)	T_{sat}	Saturation temperature of the fluid ($^\circ\text{C}$)
P	Pressure (Pa)	T_w	Test surface wall temperature ($^\circ\text{C}$)
		V	Input voltage (V)

interaction between the working fluid and the channel walls. Hence, microchannels are very effective for cooling of surfaces with high heat flux surface-densities.

Microchannel heatsinks were introduced in 1981 by Tuckerman and Pease [5]. After Tuckerman and Pease, various researchers have explored many aspects of microchannel heatsinks, and so far, many applications of these devices were filed as patents. For instance, Lee and Garimella [6] invented a high-performance microchannel heatsink for cooling microelectronic chips. In recent years, many of the microchannel studies are dedicated to nanofluid flows and heat transfer. Among them, Ho et al. [7] experimentally addressed the effect of using alumina/water nanofluid as the coolant in a copper microchannel heatsink. The outcomes indicate that using alumina/water as the working fluid improves the thermal performance of the microchannel by reducing the temperature of the heatsink and increase of convective heat transfer. However, using the alumina/water nanofluid slightly increased the required pumping power.

Considering the modeling of heat transfer in microchannels, Hatami and Ganji [8] utilized a porous media approach for the theoretical analysis of microchannel heat sinks. Vinoth and Kumar [9] investigated the heat transfer in a heatsink in the presence of oblique fins. They studied three different shapes of ribbed microchannels: semicircle, square, and trapezoidal. The results indicate that the shape of the microchannel induces a significant effect of the heat transfer. These researchers demonstrated that a trapezoidal cross-section profile results in a better heat transfer performance. Lin et al. [10] theoretically studied the flow and heat transfer in a wavy microchannel heat sink as a new microchannel heatsink. The results indicate that by changing the shape of the channels, the heat transfer can be enhanced. Yang et al. [11] analyzed the flow and heat transfer of water in microchannels experimentally and numerically. The surface of the microchannel was covered with an array of fins. Considering the forced convection boiling in microchannel heatsinks, Chen and Garimella [13] performed experiments to study boiling heat transfer of dielectric fluid in a silicon microchannel heatsink. The heatsink was made of 24 microchannels. They utilized cameras with the speed of 12,500 frames per second for visualizations purpose. The heat transfer and pressure drop were also measured in the microchannel arrays. The results indicate a bubbly flow at low heat fluxes can be seen. However, the increase of heat flux forms a vapor slugs flow in the channel. An extra increase of surface heat-flux results in alternating wispy-annular flow and churn flow in the downstream portion of the microchannel. A reversal flow was also detected next to the microchannel inlet at the upstream region of the channel. Chang and Pan [14] have experimentally investigated the instability of boiling flow heat transfer in a microchannel heatsink. The heatsink was made of 15 parallel microchannels. They have established a stability map on the plane of phase change number against inlet subcooling number.

Celata et al. [15] have studied the heat transfer characteristics of flow boiling in a single horizontal microchannel of length 102 mm with the circular cross-section of a 480 μm inner diameter and an outer diameter of 800 μm . The working fluid was FC-72 dielectric liquid.

They used a high-speed video camera to capture the flow behavior of the working fluid in the channel. The results show alternating bubbly/slug flow, slug/annular flow, and annular/mist in high heat flux and mass velocities. Ducoulombier et al. [16,17] have also studied the boiling flow and heat transfer of Carbon dioxide as the working fluid in a microchannel. Depending on the boiling number, the outcomes indicate that generally, two heat-transfer regimes are existing in the microchannel. In the case of a boiling number higher than 1.1×10^{-4} , the heat transfer coefficient was highly dependent on the heat flux and moderately influenced by the quality and the mass flux. In the case of a boiling number lower than 1.1×10^{-4} , the heat transfer coefficient is almost independent of the heat flux, but it is under the significant influence of the mass flux and the quality of the working fluid in the channel.

Fayyadh et al. [18] have adopted a multi microchannel heatsink as the test channel to study the flow boiling heat transfer of R134a refrigerant. The heatsink made of copper was constructed using 25 microchannels of a rectangular cross-section of size 300 $\mu\text{m} \times 700 \mu\text{m}$ ($W \times H$). The channels were separated using a thick wall of size 200 μm . The experiments were performed for the mass velocity in the range of 50–300 $\text{kg/m}^2\text{s}$ and surface heat flux at the basis in the range of 11.46–403.1 kW/m^2 . A high speed-camera was utilized to capture boiling behavior. The outcomes reveal that the gradual increase of the heat flux results in bubbly, slug, and wavy-annular flow patterns, respectively.

Agostini et al. [19–21] in a series of experimental studies have investigated the high heat flux boiling heat transfer characteristics of R236fa [20] and R245fa [21] refrigerants. They have also studied the boiling behavior and two-phase pressure drop of R236fa refrigerant [19] in a silicon multi-microchannels. The heatsink was composed of 67 parallel channels of size 223 μm , 680 μm and 20 mm long ($W \times H \times L$). The channels were separated using a thick wall of size 80 μm . The experiments were conducted for the surface heat flux at the basis of the microchannel in the range of 3.6–221 W/cm^2 and the mass velocity in the range of 281–1501 $\text{kg/m}^2\text{s}$. The vapor quality of the channel outlet was in the range of 2%–75%, and the working temperature was 25 $^\circ\text{C}$. The outcomes reveal that the heat transfer coefficient is an increasing function of heat flux, and usually, it is independent of the mass velocity and outlet vapor quality. Recently, Chen et al. [13,22] experimentally examined the time-periodic flow boiling heat transfer and bubble dynamics of R-134a in a narrow annular duct due to heat flux oscillation. They found that the oscillation amplitudes of the surface temperature and heat transfer coefficient increases when the boiling regime is in the persistent.

One way to further enhance the heat transfer in a microchannel is the surface modification by etching micro pin fins. In this case, in which, the microchannel is a microgap, the shape of the pin fins can control the flow and heat transfer. Few studies have addressed the effect of the shape of pin fins on the flow and heat transfer in channels. Narendran et al. [12] summarized the effect of various shapes of fins including circle, triangle, square, pentagon, and hexagon was addressed on the flow and heat transfer of boiling flow in microchannel gaps. For

example, Kosar and Peles studied the flow boiling in a microgap of a silicon channel with the obstacles of circular pin-fin [23] and hydrofoil pin-fins [24]. The gap cross-section size was $1.8 \text{ mm} \times 10 \text{ mm}$, and the height was 0.243 mm . They utilized R-123 as working. Circular [25] and square [26] pin-fin in a staggered arrangement and water as the working fluid were typical case studies. Besides, the square pin-fin with FC-72 as working fluid [27–30] were addressed. The square pin-fin with R-134a as the working fluid was also addressed [31]. Isaacs et al. [32,33] investigate the effect of R245fa as the working fluid on the flow boiling in a microgap with circular pin-fin obstacles. Recently, Woodcock et al. [34] investigated the staggered obstacles with piranha pin fin shape using HFE-7000 as the working fluid. Recently, Han et al. [40] performed an excellent review of the flow boiling heat transfer in microgaps. The outcomes indicate the promising potential of high heat flux removal of microgaps. They concluded that further fundamental researches are demanded to understand the physics of boiling in microgap.

The literature review shows that there is no study to address the boiling flow behaviors in a microgap with nucleated pin fins. The present study aims to experimentally analyze the effects of using a parallel array of nucleated columnar pin fin obstacles on the flow boiling behavior of FC-72 liquid dielectric in a microgap channel.

2. Experimental

In the present experiment, a microchannel, in which its inner surface is covered with parallel micro-fin pins, is synthesized. The boiling thermal performance and the on-boiling pressure drop are studied in the microchannel. The working fluid is adopted as FC-72 dielectric fluid due to its important practical applications in electronic cooling devices. The experimental setup is consist of a channel test module, a fluid circulation system, measurement systems, and heat exchanger cooling system. The fluid circulation system feeds the cold working fluid into the microchannel test module and sucks the mixture of liquid and vapor at the microchannel outlet. It also circulates the working fluid in heat exchanger and filters. The schematic view of the experimental setup is illustrated in Fig. 1. The test module consists of a microchannel, a very

thin plane electrical element, some sealing layers, and insulation materials. The schematic view of the test section module is depicted in Fig. 2. Fig. 3 shows a view of the synthesized microchannel with the parallel pin fins. The microchannel is almost a convergent-divergent shape rectangle, in which there is an inlet hole in one end and an outlet hole in the other end. The test section of the channel is constructed as a $10 \text{ mm} \times 10 \text{ mm}$ square surface covered with nucleated columnar fins arranged in parallel.

A machined stainless-steel basis is utilized as the basis of the test module. A thin (film) heater is placed over a thick asbestos gasket (2 mm) with a Teflon gasket layer (1 mm), which acts as the insulation substrate. An AC power-source with adjustable voltage is utilized as the power source for controlling the heating power of the element. A Teflon gasket layer seals the thin heater and the asbestos layer to prevent the heater from being exposed to the gaseous FC-72. The microchannel, made of tantalum wafer, is mounted over the substrate insulation layers. The inlet and outlet sections of the microchannel are connected to the machined stainless-steel basis using a thick rubber gasket (2 mm) as sealing. The microchannel is fixed in the middle of a basis, and a stainless-steel cap is placed at the top as a cover. There is a glass window at the cap for the test purpose. The boiling and flow behavior in the test surface can be observed through the window and captured by cameras. A layer of thermal insulation foam is utilized to cover all surfaces of the test module.

The FC-72 working flow enters the channel from an inlet port and flows in the divergent part of the channel toward the test section (covered with fins), and then FC-72 flows in the convergent part of the microchannel toward the outlet hole. A film element with high surface heat flux is placed just below the test-section part of the microchannel producing a large amount of heat. The working fluid, which flows in the microchannel, absorbs the generated heat of the element and undergoes through a phase change from liquid to vapor. The vapor and remaining hot liquid leaves the microchannel through the microchannel outlet and enters a closed type condenser to get cold and phase change to the cold liquid phase. The cold working fluid liquid leaves the condenser and enters into a $10 \mu\text{m}$ filter before reaching to a gear pump. The filter removes the undesired large particles, which may come from the

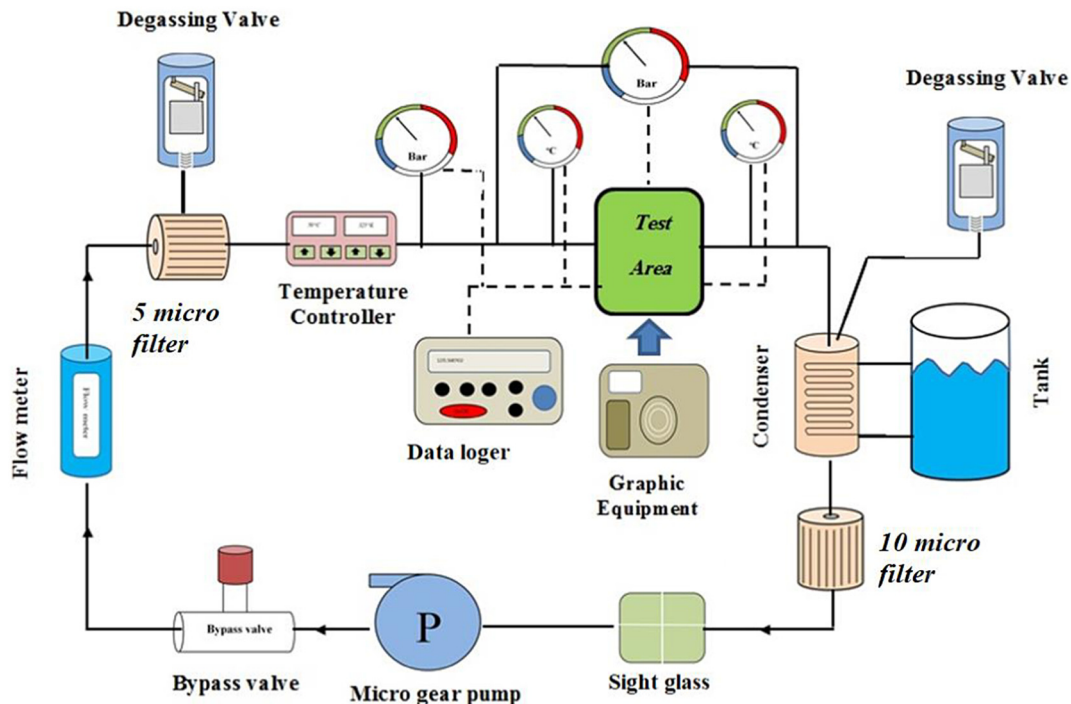


Fig. 1. Schematic view of the experimental setup.



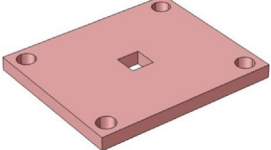
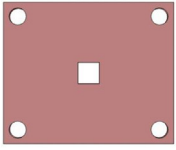
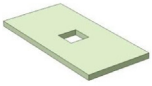

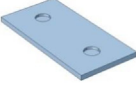

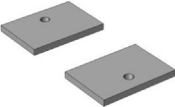

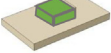

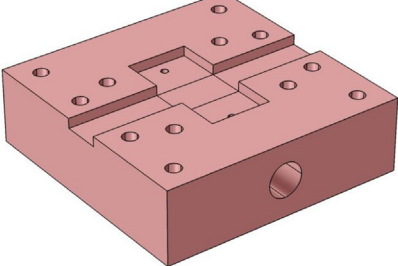
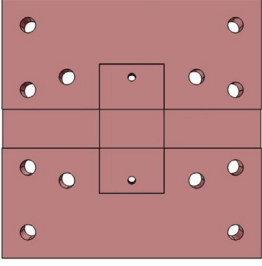
3D View	XY View	Name of structure
		M6 Screw
		Stainless steel Upper cover
		Upper gasket
		Tantalum wafer
		Lower gasket
		Film heater/Asbestos gasket
		Stainless steel basis

Fig. 2. Schematic view of the test-module section.

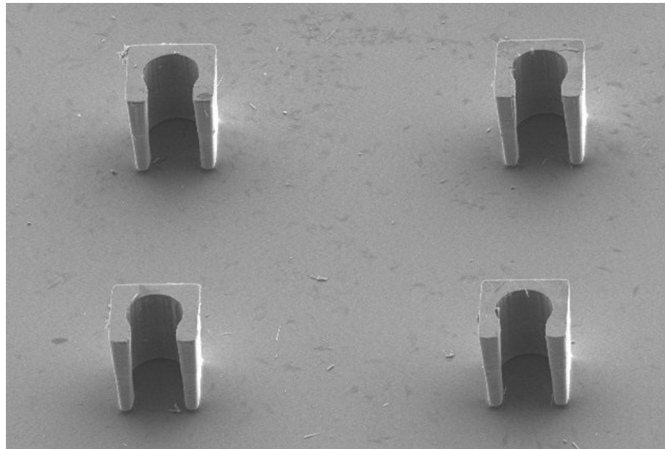


Fig. 3. Thethe test-section and columnar nucleated fins, the parallel arrangement of fins with the center-to-center distance of 400 μm .

condenser or other parts of the test setup. The gear pump receives the low-pressure cold FC-72 working fluid and increases its pressure. The high-pressure FC-72 flows through a flow meter and a 5 μm filter. The

filter is essential to capture very tiny particles, which may be released from the gear pump or other experiment parts, and it prevents them from clogging the microchannel passages. There is a temperature control system just before the test module to fine-tune the temperature of the working fluid before entering the microchannel. The measurement system consists of two pressure gauges, a flowmeter, several thermocouples, and a photograph capturing system.

The pressure gauges measure the pressure of the working fluid just before entering the microchannel and at the outlet of the microchannel to monitor the pressure drop across the microchannel test module. A float-ball type flowmeter is utilized to measure the liquid flow rate of FC-72 before entering into the microchannel. The flow rate was adjusted manually by a combination of using the bypass valve as shown in the setup diagram and adjusting the gear pump rotation. The flowmeter is utilized as the measuring device. Three thermocouples are utilized to monitor the temperatures of FC-72 before entering the microchannel. A thermocouple is placed at the outlet of the microchannel. Five thermocouples are placed at the bottom of the test-section part of the microchannel surface. The thermocouples are arranged in the equal distance in the flow direction to measure the change in the temperature of the microchannel surface along with the fluid flow. A photographing system, capable of capturing videos and high-quality pictures, and axillary light sources are utilized to observe the fluid flow behavior of FC-

72 in the test-section part of the microchannel. A data logger is utilized to receive the signals from the measuring sensors and save the data. The details of the utilized experimental setup-components and the measurement devices are summarized in Table 1.

The thickness of the microchannel is 0.1 mm, and the fins heights are made as equal to the thickness of the microchannel, 100 μm . The distance between the centers of fins is 400 μm . The test-surface of this experiment is made of 0.5 mm thick tantalum wafer. The microchannel and the nucleated fins with a depth of 100 μm are etched over the wafer. The photo of the test-surface is depicted in Fig. 3. Five thermocouple holes are drilled at the back of the wafer. The surface of the test-section above the element is covered with 613 nucleated square columnar fins of cross-section size of 100 μm . As depicted in Fig. 4, inside of each fin is nucleated with a circle size of 60 μm and an opening of 45 μm . The fins are etched in parallel with the center-to-center distance of 400 μm . The pockets are aligned opposite to the inlet flow.

It is worth mentioning that a vacuum pump is employed to evacuate impurities, water vapor, and non-condensable gases from the micro-channel cavity before commencing the experiments. As mentioned, FC-72 is adopted in the present experiment as the working fluid. FC-72 is an excellent dielectric fluid, which is a non-toxic, non-flammable, and non-electrical conductive liquid. At the atmosphere pressure, it boils at 56.6 $^{\circ}\text{C}$. Moreover, it has a very stable chemical and thermophysical properties. The thermophysical properties of this working fluid, FC-72, for various working temperatures have been reported in [35]. In the present study, two working temperatures of 35 $^{\circ}\text{C}$ and 50 $^{\circ}\text{C}$ are tested to analyze the performance of the microchannel under different thermophysical properties of FC-72. During each test, the mass flow rate of FC-72 is kept constant at a specific value, and the heat flux of the element is increased to observe the boiling convection behavior of the working fluid for two inlet temperatures of 35 $^{\circ}\text{C}$ and 50 $^{\circ}\text{C}$.

3. Analysis of experimental data

The surface heat flux of the element is calculated by dividing the actual element heat power (Q_{act}) to its surface area (A_p) as $q'' = Q_{act}/A_p$ where the actual heat power of the element is evaluated by multiplying the input current (I) by the input voltage (V) minus element loss as $Q_{act} = V \times I - Q_{loss}$. Q_{loss} is accounted for about 5% of the overall input power.

As mentioned, five thermocouples were mounted below the test-section aligned along with the flow direction. The average temperature of the five thermocouples is considered as the temperature of the test-section surface, T_{ave} . However, as there is a small thickness between the mounted places of the thermocouples and the actual surface of the test-section inside the channel, a thermal conductive correction is employed

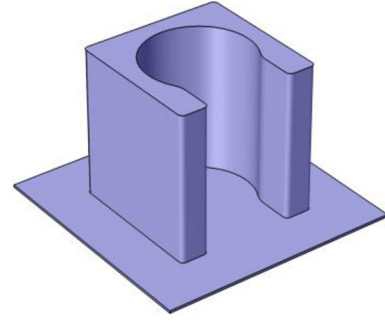


Fig. 4. The schematic view of a single nucleated column fin, the center pore size is 60 μm , and opening size is 45 μm .

Table 2

The onset boiling values and the corresponding surface heat flux for different mass flow velocities and saturation temperatures.

Mass flow velocity G (kg/m ² s)	$T_{sat} = 35^{\circ}\text{C}$			$T_{sat} = 50^{\circ}\text{C}$		
	ONB ($^{\circ}\text{C}$)	q'' (W/cm ²)	Pressure drop (kPa)	ONB	q'' (W/cm ²)	Pressure drop (kPa)
94	13.9	1.5	2.8	10.5	0.7	5.24
138	30.1	2.24	4.01	28.3	1.38	3.4

Table 3

The surface temperature difference (ΔT), the surface heat flux, and pressure difference just after ONB for different mass flow velocities and saturation temperatures.

Mass flow velocity G (kg/m ² s)	$T_{sat} = 35^{\circ}\text{C}$			$T_{sat} = 50^{\circ}\text{C}$		
	ΔT ($^{\circ}\text{C}$)	q'' (W/cm ²)	Pressure drop (kPa)	ΔT ($^{\circ}\text{C}$)	q'' (W/cm ²)	Pressure drop (kPa)
94	15.1	1.77	7.47	13.9	1.27	9.78
138	22.8	3.25	9.3	20.7	2.84	10.2

to correlate the average temperature of the test-section surface (T_{wall}) to the average temperature of thermocouples (T_{ave}) as:

$$T_{wall} = T_{ave} - q'' \times l/k \quad (1)$$

where $l = 230 \mu\text{m}$ is the thickness of the tantalum wafer between the mounting place of the thermocouples and the surface temperature, and

Table 1

The details of the experimental setup components.

Type	Production (model)	Measurement details
A pressure sensor	Cole Parmer (EJA110A)	0 to 172.36 kPa The maximum error $\pm 0.065\%$ of the maximum pressure drop, i.e., ± 0.112 kPa
Flowmeter	AALBORG (P31A4-BAO / 044-40-ST)	0–150 ml/min, the maximum error is $\pm 1.5\%$ of the maximum flow, i.e. ± 2.25 ml/min
Micro gear-pump controller	Cole Parmer (RZ-75211-10)	Used to adjust the motor speed
Micro gear-pump head	Cole Parmer (RZ-07002-26)	The output flow rate is adjusted by changing the motor speed
Thermocouples	Omega (Sheathed T-type)	The accuracy of the thermocouples is $\pm 0.5^{\circ}\text{C}$
AC transformer		The output power of 100 W used to power up the thin soft heater
Vacuum pump	ULVAC (GVD-050A)	the maximum vacuum pressure 5×10^{-4} Torr
Data logger	Agilent's data logger (34970A)	Receives the sensors data
Digital monocular camera	Nikon (D5100)	Associated with an external magnification of 1:9 microscope and a minimum working distance of 18.5 mm
A light source	Luminar Ace (LA-60Me-R)	Utilized as an auxiliary device with an input voltage of 100 VAC and a 60 W metal halide lamp with an average brightness of 2,500,000 lx
Microscope	Ching Hsing Computer-Tech Ltd. (FS-230 T)	The magnification range of 1 to 230 times and capability of five-segment zoom
Liquid flow filters	–	The filters are multi-layer 5 and 10 μm grid
Asbestos gasket	–	size of $16 \times 20 \text{ mm}^2$
Thin film heater		$10 \times 10 \times 0.5 \text{ mm}^3$
Test wafer	Tantalum	Wafer with the test surface size of $16 \times 46 \times 0.5 \text{ mm}^3$

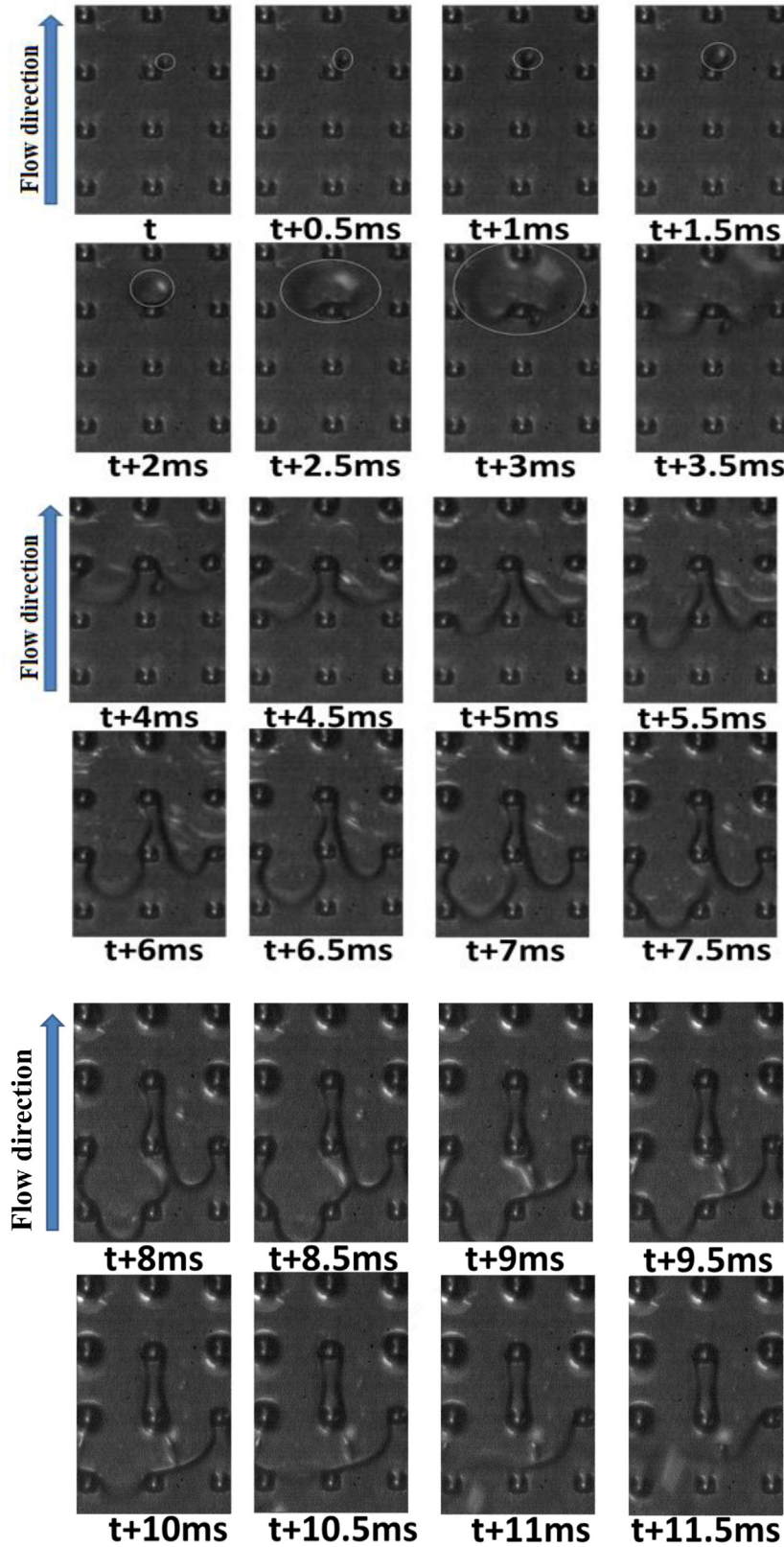


Fig. 5. The flow filed behavior of formation of bubbles at the nucleated fins when $T_{sat} = 50\text{ }^{\circ}\text{C}$, $G = 94\text{ kg/m}^2\text{ s}$ and $q'' = 0.67\text{ W/cm}^2$ and shooting speed 0.5 ms .

k denotes the thermal conductivity of the Tantalum wafer, which is about $1.24 \times 10^{-2}\text{ W/mK}$. The inlet temperature (T_{in}) of the test module is obtained as the average temperature of three thermocouples, which are mounted at the inlet section. The saturation pressure (P_{sat}) is evaluated as the average pressure of the inlet (P_i) and outlet pressure

(P_o) of the test module. Accordingly, the saturation temperature of T_{sat} is obtained using the table of properties for FC-72 reported in Carey (1992).

The convective heat transfer coefficient, h , is evaluated using the Newton's law of cooling as.

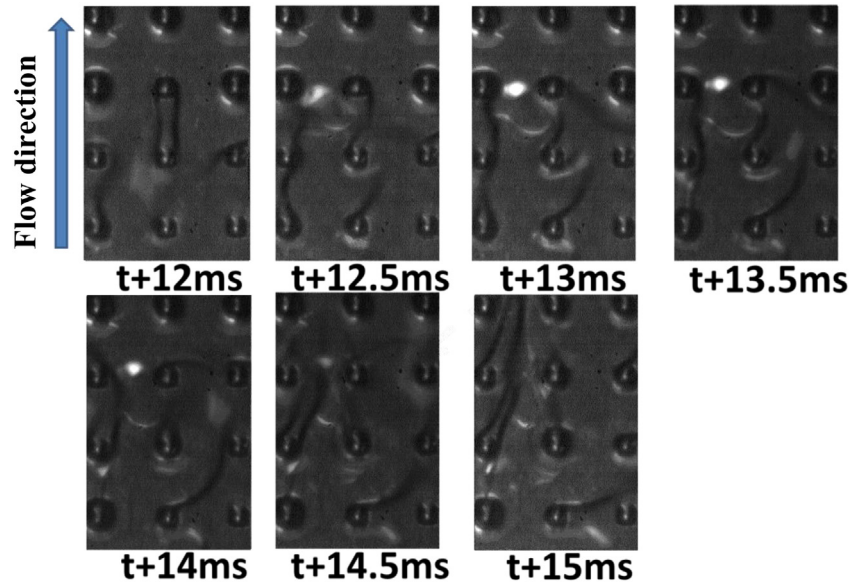
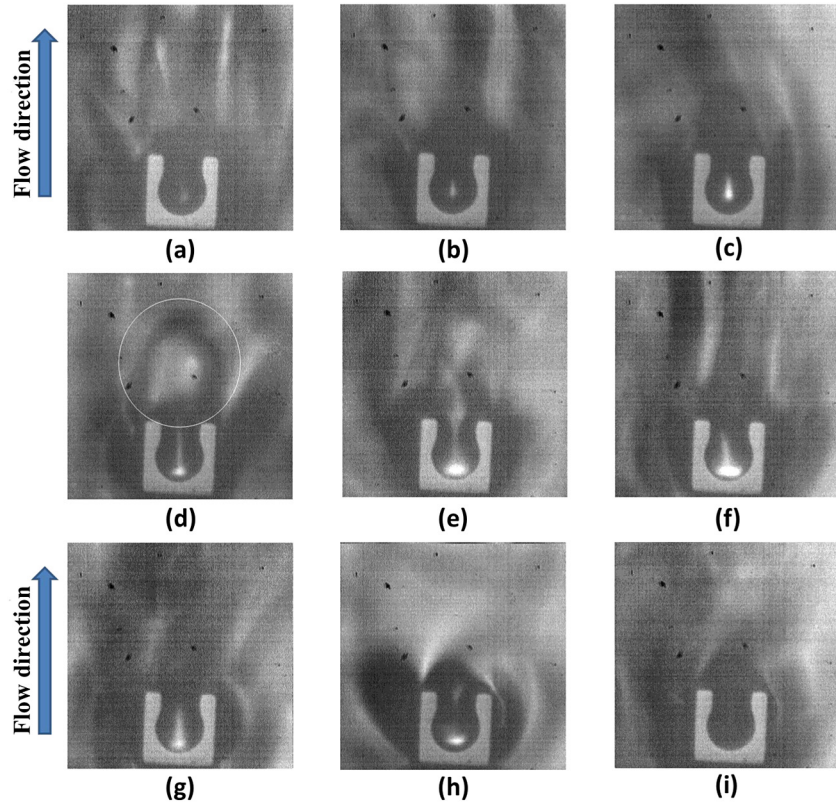


Fig. 5. (continued)

Fig. 6. The flow formation behaviour in a single pore when $T_{sat} = 50^\circ\text{C}$, $G = 94 \text{ kg/m}^2\text{s}$ and $q'' = 0.67 \text{ W/cm}^2$ and shooting speed 1200 fps.

$$h = q'' / (T_{wall} - T_{in}) \quad (2)$$

The working fluid mass-velocity that flows in the microchannel can be evaluated as:

$$G = \dot{m} / A_c \quad (3)$$

where G is the mass-velocity and \dot{m} is the mass flow rate in the channel, and A_c denotes the cross-sectional area of the microchannel at the test-section. The outlet vapor quality is evaluated by writing the energy-balance using the known net input-heat and known inlet mass flow rate as:

$$x_e = \frac{(Q - Q_{loss}) - \dot{m}c_p(T_{sat} - T_{in})}{\dot{m}h_{fg}} \quad (4)$$

where h_{fg} denotes the latent heat of phase change from the liquid to vapor.

4. Results and discussion

The experiments are performed for fixed liquid flow rates in the range of 6–30 ml/min and the mass velocity of 94–135 kg / m² s. The minimum heating rate at the test-section is 1 W. However, the

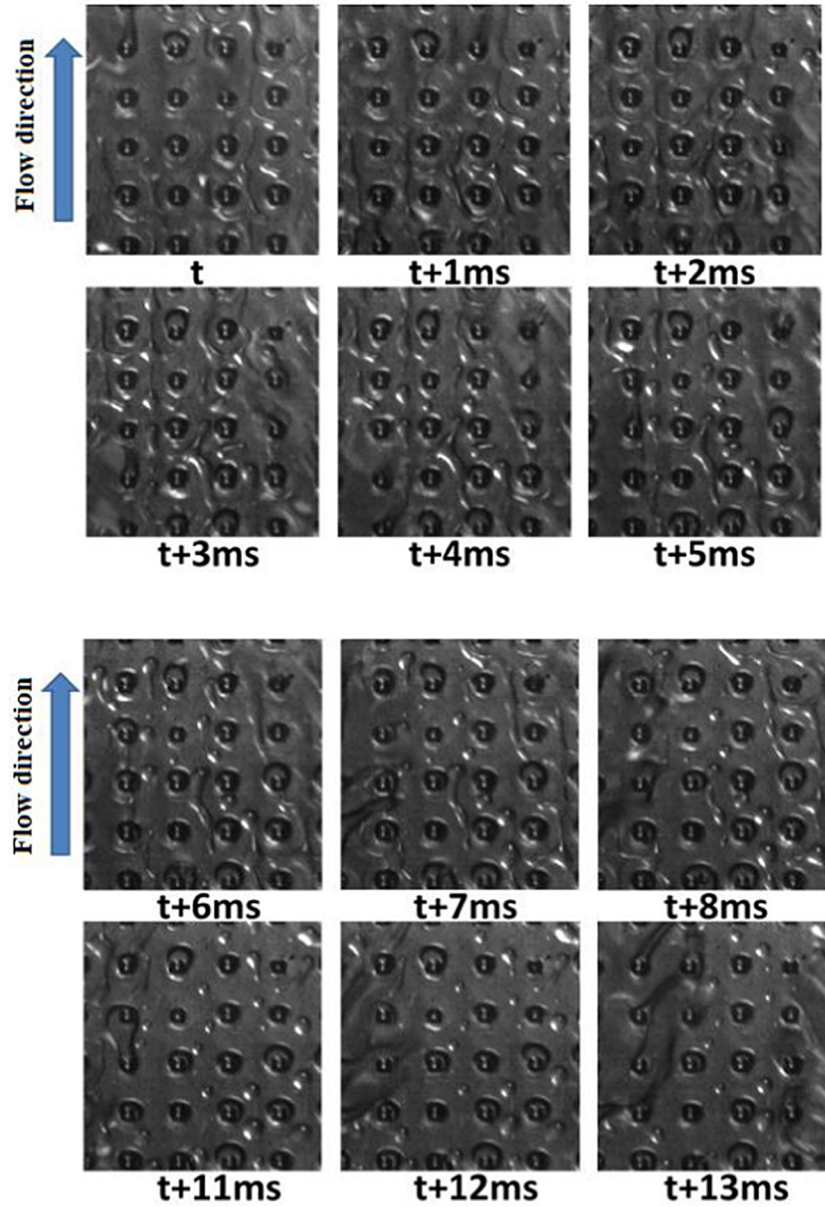


Fig. 7. Boiling flow regime when $q'' = 0.67 \text{ W/cm}^2$, $G = 94 \text{ kg/m}^2\text{s}$ and $T_{sat} = 50^\circ\text{C}$.

maximum heating rate is considered as the upper limit of these conditions: the test-surface pressure difference ($> 15 \text{ kPa}$) between inlet and outlet, or the test-section overheat ($> 100^\circ\text{C}$).

Table 2 shows the values of onset boiling temperature and the corresponding surface heat fluxes as well as the pressure drop at the test-section for two saturated temperature of $T_{sat} = 35^\circ\text{C}$ and $T_{sat} = 50^\circ\text{C}$. Table 3 shows the same results but for a case just after the onset of boiling. In Table 2, ONB indicates the onset of boiling. When the mass flow rate is low ($G = 94 \text{ kg/m}^2\text{s}$), and the saturation temperature is high ($T_{sat} = 50^\circ\text{C}$), the boiling (ONB) occurs at a temperature difference of 10.5°C . Considering the same case but a lower saturation temperature ($T_{sat} = 35^\circ\text{C}$), ONB occurs at 13.9°C .

As seen, working with a higher saturation temperature results in a lower temperature difference for the start of boiling. This difference is mainly due to the difference in the values of surface tension between the channel and fin surface and the working fluid. When the mass velocity increases to $G = 138 \text{ kg/m}^2\text{s}$, the value of ONB for the working fluid with the lower saturation temperature ($T_{sat} = 35^\circ\text{C}$) is 30.1°C , and the ONB value for the case of $T_{sat} = 50^\circ\text{C}$ increases to 28.3°C . As

the mass velocity increases, the convective heat transfer and the thermal and hydraulic interaction between the fins and the working fluid increases. Indeed, by the increase of the mass flow rate, the momentum interaction between the fluid and fins increases, and the fluid flow prevents the formation of bubbles at the surface. Hence, the boiling occurs at a higher temperature difference and a higher surface mass flux. Comparing the corresponding heat flux for ONB values in Table 2 reveals that the increase of the mass velocity increases the ONB heat flux. This is due to the increase of fluid interaction with the fins and the channel walls, which increases the convective heat transfer coefficient.

Tables 2 and 3 reveal that the pressure-drop at the subcooled flow is almost negligible, but at the beginning of boiling heat transfer, a large amount of pressure-drop up to three folds occurs. This is because the increase of the surface heat flux increases the amount of produced vapor. After the start of boiling, the pressure-drop of the fluid with higher saturation temperature, $T_{sat} = 50^\circ\text{C}$, is higher due to a substantial amount of produced vapor. The increase in the working temperature increases the pressure drop. By the increase of the working

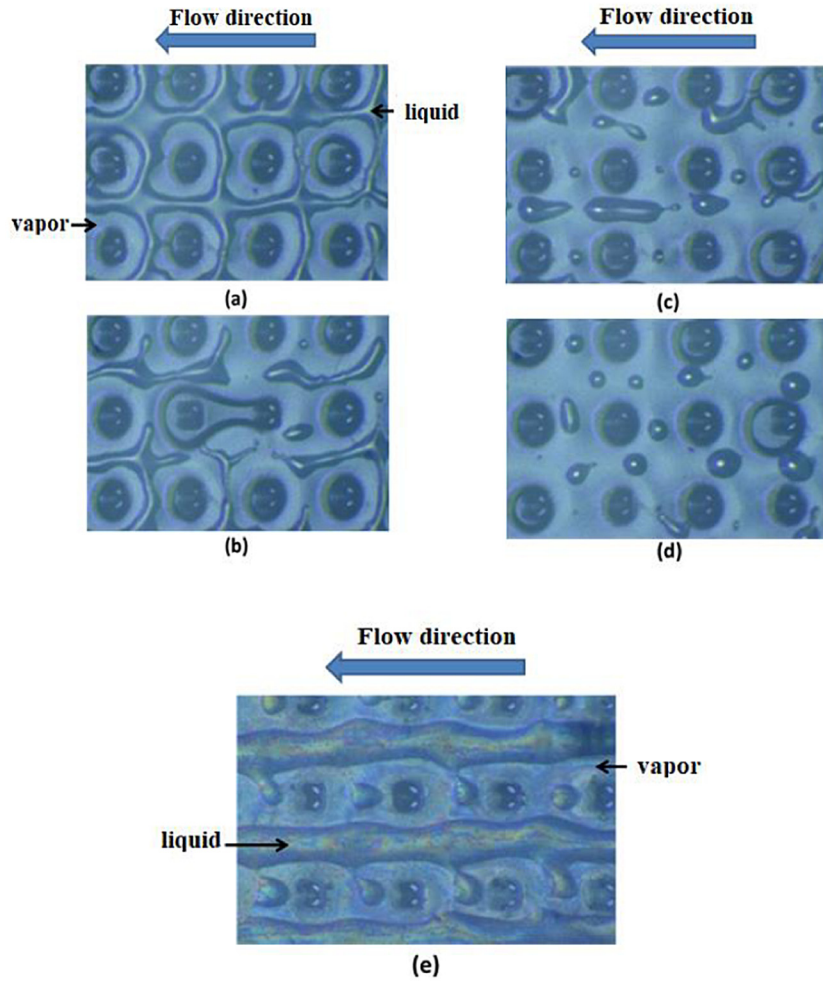


Fig. 8. Diagram of convective boiling flow regime when $G = 94 \text{ kg/m}^2 \text{ s}$, $T_{\text{sat}} = 50^\circ \text{C}$ and surface heat flux increases from 0.67 W/cm^2 to 4.5 W/cm^2 , (a) cell flow, (b) block flow, (c) droplet/block flow, (d) droplet flow, and (e) annular flow.

temperature, the difference between the enthalpy of liquid and the enthalpy of vapor decreases. Indeed, the increase in the working temperature decreases the latent heat of phase change. Therefore, at a constant heat flux, the amount of produced vapor will be higher at a higher working temperature.

In this experiment, a high-speed camera is used to capture the bubble nucleation flow field during the initial boiling of FC-72 at the test-section. The results are reported for the case of $T_{\text{sat}} = 50^\circ \text{C}$ and mass velocity of $94 \text{ kg/m}^2 \text{ s}$ when the surface heat flux is kept constant at 0.67 W/cm^2 . Fig. 5 illustrates the systematic formation of bubbles at the nucleated column fins. The shooting time interval between each picture is 0.5 ms . The arrow next to each set of figures denotes the flow direction. As seen in Fig. 5, at the beginning (at the time t), the bubble is generated at the edge of a nucleated fin pore. Then it expands toward the downstream and the adjacent fins to form a massive vapor bubble during the time interval of t to $t + 3 \text{ ms}$. Then, during the time interval of $t + 3.5 \text{ ms}$ to $t + 8.5 \text{ ms}$, the vapor expands toward the upstream until it occupies most of the test surface and surrounds the column fins. So that, the residual liquid inside and around the pores of the column fin are surrounded by vapor. During the time interval of $t + 9 \text{ ms}$ to $t + 11 \text{ ms}$, sometimes, a single column fin is surrounded by vapor, and sometimes, two fins are surrounded by vapor. When the liquid continues to enter the test surface, it pushes some of the vapor toward the downstream and outlet. During $t + 11.5 \text{ ms}$ to $t + 13 \text{ ms}$, the remaining liquid next to the pores absorbs the heat of column pores and commences to expand by generating vapor. Then, during $t + 13.5 \text{ ms}$ to $t + 15 \text{ ms}$, the vapor occupies most of the test-section, and again, the

cycle repeats.

After the pores of the columnar fins and the surrounding residual liquid are surrounded by vapor, the liquid still wets the pores and the fins also absorb the heat from the heating element in beneath of the test-section, and hence, new bubbles continue to generate. In this experiment, the single pore nucleation process is captured using the video recording device with the shooting speed of 1200 fps . The results are reported in Fig. 6. In this figure, the arrow shows the flow direction. As shown in Fig. 6 (a), at the beginning, the pores are wetted by the liquid. At this time, the heating element is on, and the fins are hot. The column fins continue to absorb the heat from the basis of the heatsink, which is mounted above the film element, and hence, some vapor is generated inside the pores. Figs. 6 (b–h). As the pores are positioned against the flow direction, the pressure in the pore structure is higher than the pressure at its opening. The pressure difference between the pore structure and the pore opening is greater than the surface tension, and hence, as seen in Fig. 6 (d), the bubble emerges from the pore. The bubbles continue to increase to reach the point of the separation from the pore and combine with the surrounding gas. The bubbles start to cool down as they leave the pore opening by heat transfer to the surrounding. Finally, as depicted in Fig. 6 (i), the liquid fills the area occupied with the first bubble, and the cycle continues to be repeated. It is worth noticing that the pores provide a stagnant space and allow the liquid to absorb the heat and change phase into the vapor. The formation of the vapor disturbs the fluid and increases the heat transfer. Indeed, the pores are the source of the formation of the bubbles. In a case of the reverse flow directing, the pores provide a stagnant space for

vapor formation, but the release of the vapor would be in the opposite direction of flow, which suppresses the formation of the vapor.

Fig. 7 shows the flow regime of boiling convective heat transfer when $q'' = 0.67 \text{ W/cm}^2$, $G = 94 \text{ kg/m}^2 \text{ s}$, and $T_{\text{sat}} = 50^\circ\text{C}$. This figure depicts that as the liquid enters the test-section and fills around the column fins. The boiling readily commences around the columnar fins. So that, the vapor surrounds the pores containing the liquid, and then, the incoming liquid flows through a small gap caused by the vapor extrusion, resulting in, many small liquid branches paths that they form a cell-like shape ($t \sim t + 2 \text{ ms}$). As the liquid continues to boil and evaporate, the branched liquid paths gradually get thin until they break apart. At this time, they form a slug flow ($t + 3\text{--}5 \text{ ms}$). Then, the block of liquid continues to shrink and transforming into droplets/blocks coexisting ($t + 6\text{--}10 \text{ ms}$). Finally, the liquid becomes only tiny droplets in the flow field. At this time, the droplet flow exists when most of the flow field is in vapor state ($t + 11\text{--}13 \text{ ms}$). The upstream liquid fills into the test surface, and the boiling cycle will be repeated.

Fig. 8 shows the flow regime diagram during boiling at the mass velocity of $G = 94 \text{ kg/m}^2 \text{ s}$ and $T_{\text{sat}} = 50^\circ\text{C}$. The results are reported for the increase of the surface heat flux from $q'' = 0.67 \text{ W/cm}^2$ to 4.5 W/cm^2 . The flow-regime transformation process, depicted in Figs. 8 (a)–(d), are the cell flow and the block flow, and the droplet/block flow, and droplet flow, respectively when the heat flux increases gradually. In the case of 4.5 W/cm^2 , which corresponds to Fig. 8 (e), the heat flux is high, and hence, the boiling frequency is faster. By the increase of the heat flux, more energy is available to be absorbed by the liquid. The charging of fluid and detaching of bubbles occurs quickly, and the boiling process repeated faster. Hence, the fluctuations and boiling frequency are higher. The flow around the downstream-fins is in a vapor state, and hence, most of the liquid entering the test-section forms channels shapes to pass between the fins. The flow field forms a liquid-vapor diversion multiple independent flow channels. As can be seen in Fig. 8 (e), the flow field patterns are in the form of annular flow.

5. Conclusion

The boiling flow and heat transfer of FC-72 in the rectangular section of a microchannel is studied experimentally. An experimental setup consisting of a test module, a circulation system, and a measurement system is utilized to perform the experiments. The surface temperature difference is investigated using characteristics curves. The flow field behavior of FC-72 is observed and explored using captured images in the test-section of the microchannel. The primary outcomes of the study can be summarized as follows:

- 1- The increase of the saturation temperature decreases the onset boiling temperature difference between the inlet temperature and the test-section surface. Besides, the increase of the mass velocity increases ONB temperature difference.
- 2- The bubbles are generated at the edge of a nucleated fin pore at the start of boiling. Then, some vapor forms inside the nucleation holes, which then ejects into the flow stream. The vapor eventually forms a large vapor block surrounding a fin. The formation of bubbles shows cyclic behavior.
- 3- The pressure drop at the subcooled flow, in which the working fluid is in liquid form, is negligible. The presence of boiling heat transfer results in a large amount of pressure drop. The boiling pressure drop is up to three folds of the subcooled pressure-drop. Also, the increase in saturation temperature increases the pressure drop.
- 4- By the gradual increase of the surface heat flux at the test section, cell flow, block flow, droplet/block flow, droplet flow, and annular flow patterns can be observed.

As mentioned, the results of the present study show that the increase of mass velocity increases the temperature difference between the test-section temperature and the inlet saturated temperature of the working

fluid. This is because of the critical role of forced convective heat transfer in the channel. However, the increase of the mass velocity also increases the ONB corresponding surface heat flux. Hence, in a case with constant heat flux, the increase of mass velocity decreases the surface temperature in the absence of the boiling heat transfer. This is one of the main advantages of phase-change for forced convection heat transfer in microchannels. This advantage is important as in the case of pool boiling the subcooled temperature difference can gradually increase without boiling.

In the present study, the fins opening is aligned opposite to the flow direction, and the fins are arranged in a parallel array. In future studies, the effect of different fin opening alignments and a segregated array of fins on the boiling convection heat transfer can be investigated.

Acknowledgements

The authors appreciate the financial support from Ministry of Science and Technology, Taiwan, under grant number MOST 101-2221-E-027-044-MY2. The authors also appreciate the financial support by the “Research Center of Energy Conservation for New Generation of Residential, Commercial, and Industrial Sectors” from The Featured Areas Research Center Program within the framework of the Higher Education Sprout Project by the Ministry of Education (MOE) in Taiwan.

References

- [1] R.E. Hardesty, Micro-channel pulsating heat pipe, Google Patents, 2014.
- [2] P. Barletta, L. Diehl, M.T. North, B. Yang, N. Baldasaro, D. Temple, Advanced thermal management of high-power quantum cascade laser arrays for infrared countermeasures, Technologies for Optical Countermeasures XIV, International Society for Optics and Photonics, 2017 (1043508).
- [3] D.J. Meadowcroft, R.G. Ritter, P. Wen, H. Xu, Methods, devices and systems that dissipate heat and facilitate optical alignment in optical communications modules, Google Patents, 2017.
- [4] J.J. Lacey, A. Joshi, V. Ryali, S. Bhat, System and method for thermal management of a CT detector, Google Patents, 2017.
- [5] D.B. Tuckerman, R.F. Pease, Microcapillary thermal Interface technology for VLSI packaging, VLSI Technology, 1983. Digest of Technical Papers. Symposium on, IEEE, 1983, pp. 60–61.
- [6] P.-S. Lee, S.V. Garimella, Microchannel heat sink, Google Patents, 2007.
- [7] C.J. Ho, L. Wei, Z. Li, An experimental investigation of forced convective cooling performance of a microchannel heat sink with Al₂O₃/water nanofluid, J. Appl. Therm. Eng. 30 (2–3) (2010) 96–103.
- [8] M. Hatami, D. Ganji, Thermal and flow analysis of microchannel heat sink (MCHS) cooled by cu–water nanofluid using porous media approach and least square method, J. Energy Convers. Manage. 78 (2014) 347–358.
- [9] R. Vinoth, D.S. Kumar, Channel cross section effect on heat transfer performance of oblique finned microchannel heat sink, J. Int. Comm. Heat Mass Trans. 87 (2017) 270–276.
- [10] L. Lin, J. Zhao, G. Lu, X.D. Wang, W.M. Yan, Heat transfer enhancement in microchannel heat sink by wavy channel with changing wavelength/amplitude, Int. J. Therm. Sci. 118 (2017) 423–434.
- [11] D. Yang, Y. Wang, G. Ding, Z. Jin, J. Zhao, G. Wang, Numerical and experimental analysis of cooling performance of single-phase array microchannel heat sinks with different pin-fin configurations, J. Appl. Therm. Eng. 112 (2017) 1547–1556.
- [12] G. Narendran, N. Gnanasekaran, D.A. Perumal, A review on recent advances in microchannel heat sink configurations, J. Recent Patents Mech. Eng. 11 (3) (2018) 190–215.
- [13] C. Chen, T. Lin, W.M. Yan, Bubble characteristics in time periodic saturated flow boiling of R-134a in a narrow annular pipe due to heat flux oscillation, J. Int. J. Heat Mass Trans. 102 (2016) 1150–1158.
- [14] K. Chang, C. Pan, Two-phase flow instability for boiling in a microchannel heat sink, J. Int. J. Heat Mass Trans. 50 (11–12) (2007) 2078–2088.
- [15] G.P. Celata, S.K. Saha, G. Zummo, D. Dossevi, Heat transfer characteristics of flow boiling in a single horizontal microchannel, J. Int. J. Therm. Sci. 49 (7) (2010) 1086–1094.
- [16] M. Ducoulombier, S. Colasson, J. Bonjour, P. Haberschill, Carbon dioxide flow boiling in a single microchannel—part I: pressure drops, J. Exp. Therm. Fluid Sci. 35 (4) (2011) 581–596.
- [17] M. Ducoulombier, S. Colasson, J. Bonjour, P. Haberschill, Carbon dioxide flow boiling in a single microchannel—part II: heat transfer, J. Exp. Therm. Fluid Sci. 35 (4) (2011) 597–611.
- [18] E.M. Payyadh, M.M. Mahmoud, K. Sefiane, T. Karayiannis, Flow boiling heat transfer of R134a in multi microchannels, J. Int. J. Heat Mass Trans. 110 (2017) 422–436.
- [19] B. Agostini, R. Revellin, J.R. Thome, M. Fabbri, B. Michel, D. Calmi, U. Kloter, High

- heat flux flow boiling in silicon multi-microchannels—part III: saturated critical heat flux of R236fa and two-phase drops, *J Int. J. Heat Mass Trans.* 51 (21–22) (2008) 5426–5442.
- [20] B. Agostini, J.R. Thome, M. Fabbri, B. Michel, D. Calmi, U. Kloter, High heat flux flow boiling in silicon multi-microchannels—part I: heat transfer characteristics of refrigerant R236fa, *J Int. J. Heat Mass Trans.* 51 (21–22) (2008) 5400–5414.
- [21] B. Agostini, J.R. Thome, M. Fabbri, B. Michel, D. Calmi, U. Kloter, High heat flux flow boiling in silicon multi-microchannels—part II: heat transfer characteristics of refrigerant R245fa, *J Int. J. Heat Mass Trans.* 51 (21–22) (2008) 5415–5425.
- [22] C. Chen, T. Lin, W.-M. Yan, Experimental study on time periodic evaporation heat transfer of R-134a in annular ducts due to wall heat flux oscillation, *J Int. J. Heat Mass Trans.* 106 (2017) 1232–1241.
- [23] A. Koşar, Y. Peles, Convective flow of refrigerant (R-123) across a bank of micro pin fins, *J Int. J. Heat Mass Trans.* 49 (17–18) (2006) 3142–3155.
- [24] A. Koşar, Y. Peles, Boiling heat transfer in a hydrofoil-based micro pin fin heat sink, *J Int. J. Heat Mass Trans.* 50 (5–6) (2007) 1018–1034.
- [25] S. Krishnamurthy, Y. Peles, Flow boiling of water in a circular staggered micro-pin fin heat sink, *J Int. J. Heat Mass Trans.* 51 (5–6) (2008) 1349–1364.
- [26] W. Qu, A. Siu-Ho, Experimental study of saturated flow boiling heat transfer in an array of staggered micro-pin-fins, *J Int. J. Heat Mass Trans.* 52 (7–8) (2009) 1853–1863.
- [27] Y. Lie, J. Ke, W. Chang, T. Cheng, T. Lin, Saturated flow boiling heat transfer and associated bubble characteristics of FC-72 on a heated micro-pin-finned silicon chip, *J Int. J. Heat Mass Trans.* 50 (19–20) (2007) 3862–3876.
- [28] A. Ma, J. Wei, M. Yuan, J. Fang, Enhanced flow boiling heat transfer of FC-72 on micro-pin-finned surfaces, *J Int. J. Heat Mass Trans.* 52 (13–14) (2009) 2925–2931.
- [29] M. Yuan, J. Wei, Y. Xue, J. Fang, Subcooled flow boiling heat transfer of FC-72 from silicon chips fabricated with micro-pin-fins, *J Int. J. Heat Mass Trans.* 48 (7) (2009) 1416.
- [30] D. Guo, J. Wei, Y. Zhang, Enhanced flow boiling heat transfer with jet impingement on micro-pin-finned surfaces, *J Appl. Therm. Eng.* 31 (11–12) (2011) 2042–2051.
- [31] T. David, D. Mendler, A. Mosyak, A. Bar-Cohen, G. Hetsroni, Thermal management of time-varying high heat flux electronic devices, *J J. Electr. Packag.* 136 (2) (2014) 021003.
- [32] S.A. Isaacs, Y. Joshi, Y. Zhang, M.S. Bakir, Y.-J. Kim, Two-phase flow and heat transfer in pin-fin enhanced micro-gaps with non-uniform heating, ASME 2013 4th International Conference on Micro/Nanoscale Heat and Mass Transfer, American Society of Mechanical Engineers, 2013(V001T012A003-V001T012A003).
- [33] S.A. Isaacs, Y.-J. Kim, A.J. McNamara, Y. Joshi, Y. Zhang, M.S. Bakir, Two-phase flow and heat transfer in pin-fin enhanced micro-gaps, Thermal and Thermomechanical Phenomena in Electronic Systems (ITherm), 2012 13th IEEE Intersociety Conference on, IEEE, 2012, pp. 1084–1089.
- [34] C. Woodcock, X. Yu, J. Plawsky, Y. Peles, Piranha pin fin (PPF)—advanced flow boiling microstructures with low surface tension dielectric fluids, *J Int. J. Heat Mass Trans.* 90 (2015) 591–604.
- [35] V.P. Carey, *Liquid Vapor Phase Change Phenomena: An Introduction to the Thermophysics of Vaporization and Condensation Processes in Heat Transfer Equipment*, CRC Press, 2018.